

Magnetic evidence for an extended hydrogen exosphere at Mercury

Daniel Schmid (✉ daniel.schmid@oeaw.ac.at)

Space Research Institute, Austrian Academy of Sciences <https://orcid.org/0000-0001-7818-4338>

Ferdinand Plaschke

Austrian Academy of Sciences <https://orcid.org/0000-0002-5104-6282>

Nikolay Erkaev

Institute of Computational Modelling SB RAS

Martin Volwerk

Space Research Institute, Austrian Academy of Sciences

Wolfgang Baumjohann

Space Research Institute, Austrian Academy of Sciences

Yasuhito Narita

Space Research Institute, Austrian Academy of Sciences

Brian Anderson

The Johns Hopkins University Applied Physics Laboratory

Helmut Lammer

Austrian Academy of Sciences, Space Research Institute

Article

Keywords: extended hydrogen exosphere, Mercury, magnetic evidence

Posted Date: October 14th, 2020

DOI: <https://doi.org/10.21203/rs.3.rs-90259/v1>

License:   This work is licensed under a Creative Commons Attribution 4.0 International License.

[Read Full License](#)

Magnetic evidence for an extended hydrogen exosphere at Mercury

D. Schmid^{*1}, F. Plaschke¹, N. V. Erkaev², M. Volwerk¹, W. Baumjohann¹, Y. Narita¹,
B. J. Anderson³ and H. Lammer¹

¹ *Space Research Institute, Austrian Academy of Sciences, Graz, Austria*

(Daniel.Schmid@oeaw.ac.at)

² *Institute of Computational Modelling SB RAS, Krasnoyarsk, Russian Federation*

³ *The Johns Hopkins University Applied Physics Laboratory, Laurel, Maryland, USA*

Summary

Remote sensing observations of the Mariner 10 and MESSENGER spacecraft have shown the existence of atomic (H) and molecular (H₂) hydrogen in the exosphere around Mercury. However, to date the hydrogen number densities could only be estimated indirectly from exospheric models, based on Lyman- α radiances for H and the H₂ detection threshold of the Mariner 10 occultation experiment. Here we show the first in-situ measured altitude-density profile of atomic H, derived from magnetic field observations by MESSENGER. Our results reveal an extended H corona with densities decreasing from 1000 – 100 cm⁻³ between 2 – 8 Mercury radii. These densities are 2-3 orders of magnitude larger than previously predicted, but in good agreement with the Lyman- α radiances. The large H densities result from the dissociation of H₂. We can reproduce the observed H densities using an exospheric model which includes ionization, dissociation and recombination, that allows us to constrain the H₂ surface density to $\sim 5 \times 10^5$ cm⁻³. This is two orders of magnitude smaller than the previously assumed upper limit.

22 Introduction

23 Mercury, the innermost planet of our solar system, is surrounded by a tenuous exosphere containing
24 a variety of species that originate from the solar wind, micrometeorites and the planetary surface.
25 Atomic hydrogen was one of the first exospheric species detected by the Mariner 10 spacecraft in
26 1974, based on Lyman- α emissions [4]. Four decades later the detection of the hydrogen exosphere
27 was confirmed by Ultraviolet Visible Spectrometer (UVVS [32]) observations of the MErcury Sur-
28 face, Space ENvironment, GEophysics and Ranging (MESSENGER [40]) spacecraft [44, 45, 46].
29 The measured radiances are related to the total number of Lyman- α photons emitted along the
30 line of sight, to obtain the respective column density of the emitting hydrogen. By taking different
31 lines-of-sight, it is possible to determine the exospheric column hydrogen density as a function of
32 altitude. However, to obtain hydrogen number density profiles the measured column densities need
33 to be compared with the output of exospheric models [6, 3, 51, 25, 35, 52, 50, 24]. Early models
34 that are fitted to the measured hydrogen radiances yield maximum atomic (H) and molecular (H₂)
35 hydrogen densities near Mercury's surface of $< 1000 \text{ cm}^{-3}$ and $< 2 \times 10^6 \text{ cm}^{-3}$, respectively [29].
36 Later studies derived 1 – 2 orders of magnitude lower H surface densities [21, 44]. Based on the
37 detection threshold of the Mariner 10 occultation experiment [5], an upper limit of the H₂ surface
38 density of $\leq 2.6 \times 10^7 \text{ cm}^{-3}$ was derived [21, 28].

39 To date, the neutral hydrogen exosphere has only been measured remotely. In this study we
40 determine for the first time the local H density profile from in-situ magnetic field observations.
41 We survey the magnetic field data of MESSENGER in the solar wind for ion cyclotron waves
42 (ICWs), which are generated by freshly ionized H atoms. As the neutral H atoms from Mercury's
43 exosphere become photoionized they are picked-up by the solar wind. The new-born ions and
44 the solar wind form an unstable distribution in phase space that can produce different plasma
45 waves via resonant and non-resonant instabilities [17]. As has already been shown at Mars and
46 Venus, most prominently ICWs are excited by this instability [31, 37, 11]. ICWs are transverse
47 electromagnetic waves near the proton cyclotron frequency. They propagate nearly parallel to the
48 background magnetic field and are either left- or right-hand elliptically polarized: Theory suggests
49 that left-hand polarized waves are produced by a perpendicular pick-up geometry (background
50 magnetic field perpendicular to the plasma flow). Right-hand polarized waves are produced by
51 a parallel pick-up geometry (background magnetic field parallel to the plasma flow) [48, 49]. At
52 Mercury mainly parallel pick-up takes place, due to the small angle between the interplanetary

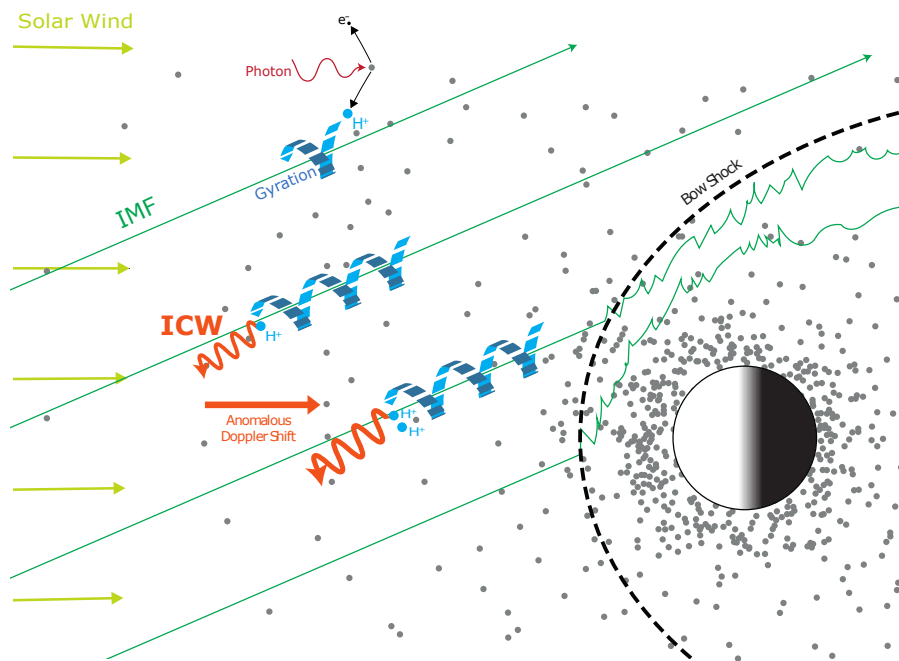


Figure 1: Illustration of ion cyclotron waves (ICWs, orange lines) generated by the gyration (blue lines) of protons (H^+ , blue dots) around the interplanetary magnetic field (IMF, green lines), which are created by photoionization of atomic hydrogen (H, grey dots).

53 magnetic field (IMF) and the solar wind streaming direction which is typically $\sim 20^\circ$ [39]. The
 54 right-hand polarized waves propagate in sunward direction with a phase speed on the order of the
 55 Alfvén velocity. That speed is slower than the solar wind velocity. Hence, the waves are carried
 56 in anti-sunward direction over the spacecraft, thereby reversing the right-hand polarization by the
 57 anomalous Doppler shift [30]: Consequently, in the spacecraft frame a left-hand polarization is
 58 observed. In that frame, the waves are shown to be always observed at the local ion gyrofrequency
 59 [11].

60 Figure 1 shows an illustration of ICWs generated by proton pick-up. The neutral hydrogen in
 61 the Mercury’s exosphere becomes photoionized first, then the new-born protons are accelerated by
 62 the convection electric field and start to gyrate around the background magnetic field (IMF) and
 63 excite the ICWs.

64 To identify ICWs which are specifically generated by the pick-up of freshly ionized planetary
 65 hydrogen, we search for time intervals with large transverse magnetic field fluctuations, which are

66 left-hand polarized in the spacecraft frame, and close to the local proton frequency. From the
67 observed wave power we are able to derive, for the first time, atomic H density profile from in-
68 situ spacecraft measurements at Mercury. These densities are 2 to 3 orders of magnitude larger
69 than previously predicted. We introduce an exospheric model, including hydrogen photochemistry,
70 that can explain the origin of the discovered extended atomic H corona. This model allows us to
71 constrain the so far unknown and overestimated H₂ surface number density to $\sim 5 \times 10^5 \text{ cm}^{-3}$,
72 which is 2 orders of magnitude lower than previously reported.

73 Results

74 Based on an automatic search algorithm, with specific selection criteria for ICWs generated by the
75 pick-up of planetary protons, we identify 2247 ICWs during 4 years of MESSENGER solar wind
76 observations upstream of the Mercury terminator. These 2247 ICWs yield the starting dataset for
77 this study.

78 ICWs should be generated locally through initial ionization of the neutral atomic H. To test
79 this, we transform the observation locations into electromagnetic coordinates to examine possible
80 asymmetries with respect to the convection electric field. ICWs propagate with speeds that are on
81 the order of (or lower than) the local Alfvén velocity (V_A), which should be much lower than the
82 injection speed (V_{inj}) [10]. Thus, we also evaluate the V_A/V_{inj} ratios during the ICWs detection.
83 Since the initial velocity of the neutral hydrogen before ionization is negligible in the planetary
84 frame, we assume that the injection velocity of the new-born ions is the solar wind velocity in the
85 solar wind frame of reference.

86 Figure 2(a) shows the position of the 2247 ICWs in the local electromagnetic coordinate system:
87 X_{MBE} points sunward, opposite to the solar wind velocity (\mathbf{V}_{inj}), Y_{MBE} is positive in the direction
88 of the background magnetic field (\mathbf{B}_0) component, perpendicular to X_{MBE} , and the Z_{MBE} axis is
89 positive in the direction of the convection electric field ($\mathbf{E} = \mathbf{V}_{\text{inj}} \times \mathbf{B}_0$). Clearly, ICWs occur at
90 large positive X_{MBE} and are evenly distributed between $\pm Z_{\text{MBE}}$, indicating local generation [11].
91 Panel (b) depicts the normalized occurrence rate of the estimated V_A/V_{inj} ratios. The histogram
92 confirms the second assumption: The Alfvén velocity is significantly smaller than the injection
93 velocity of the new born ions into the background (solar wind) plasma. From the results in Figure
94 2 we conclude that the underlying assumptions for reliable density estimations are fulfilled.

95 From the observed wave power of the ICWs we derive the required pick-up proton densities

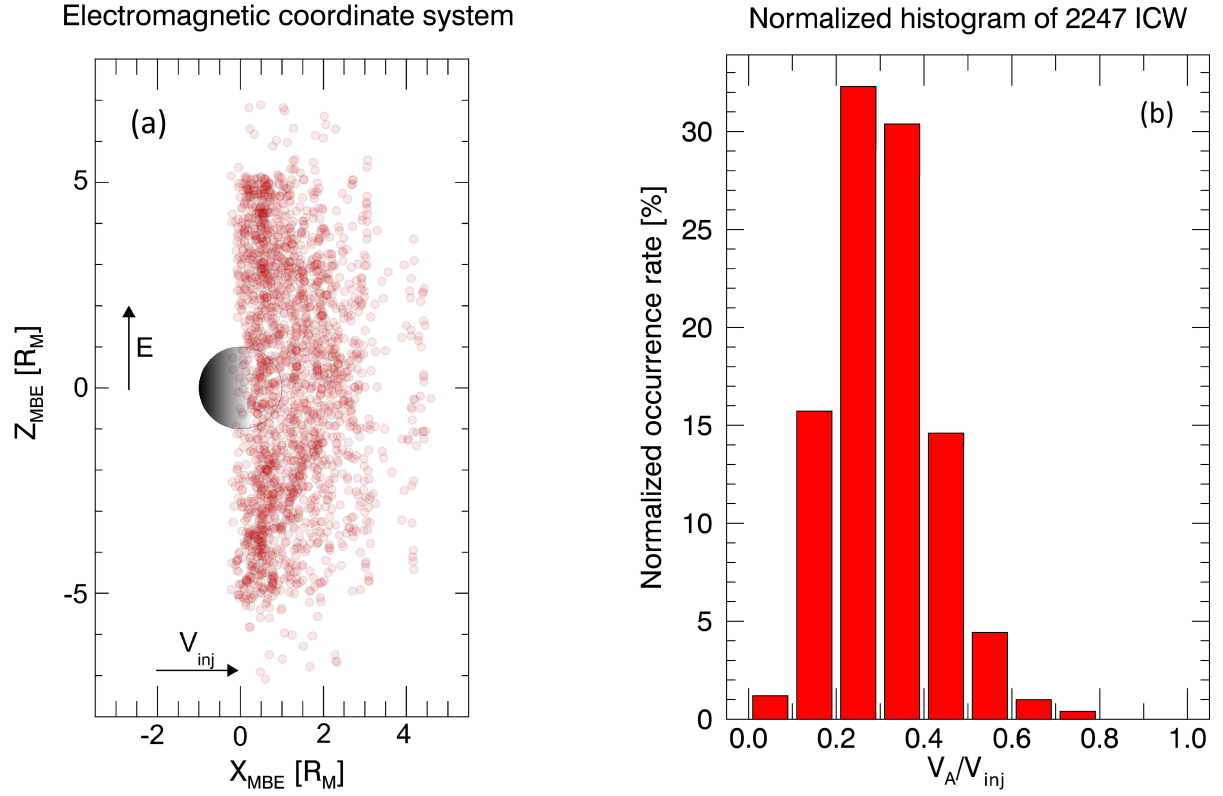


Figure 2: Panel (a) shows the position of the 2247 ion cyclotron waves (ICWs) in electromagnetic coordinates: X_{MBE} points sunward opposite to the solar wind velocity \mathbf{V}_{inj} , Y_{MBE} is positive in direction of the mean magnetic field \mathbf{B}_0 component perpendicular to X_{MBE} , and the Z_{MBE} axis is positive in direction of the convection electric field $\mathbf{E} = \mathbf{V}_{\text{inj}} \times \mathbf{B}_0$. Panel (b) shows the normalized occurrence rate of estimated V_A/V_{inj} ratios.

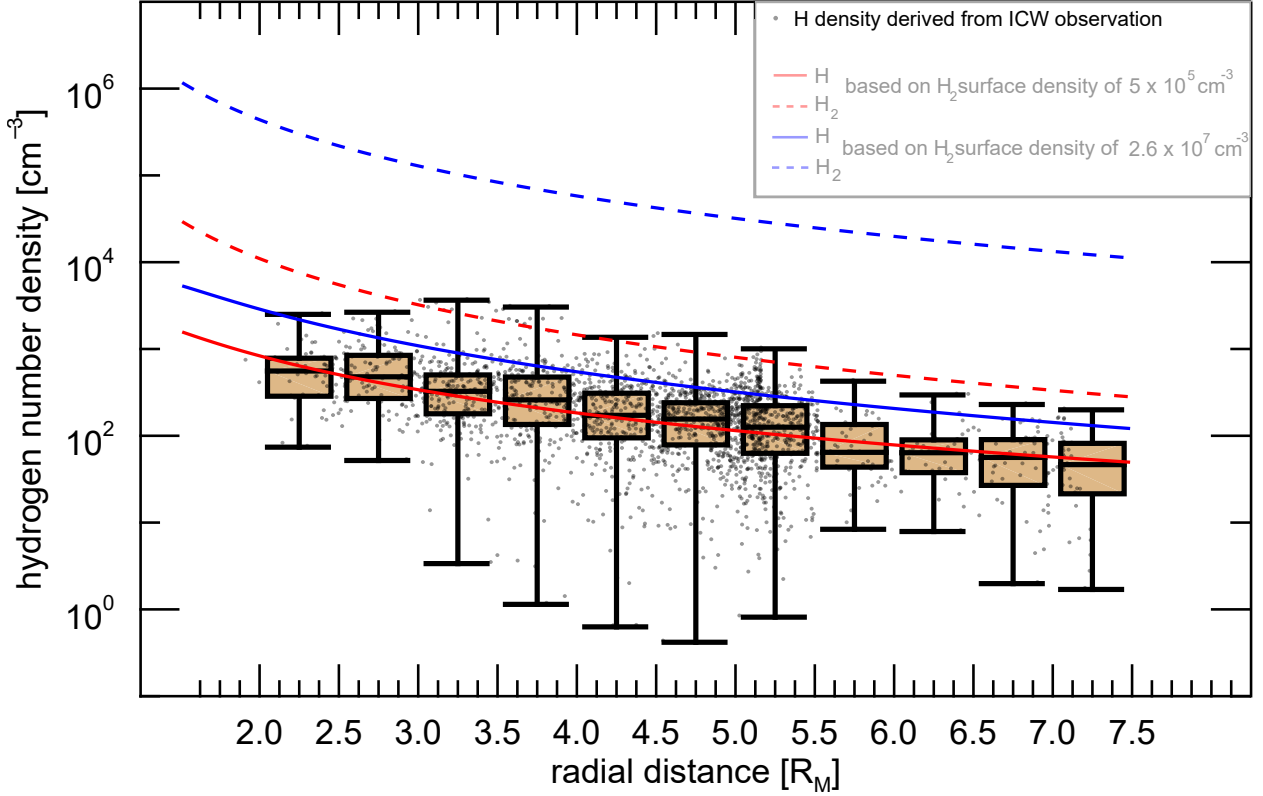


Figure 3: Boxplot of the estimated hydrogen densities as a function of the radial observation distance. The black error bar indicate the minimum and maximum number density within each $0.5 R_M$ bin. The boxes indicate the lower and upper quartiles and the horizontal black lines the median number density of each bin. The gray dots depict the derived hydrogen number densities of the 2247 ICW events. The blue and red lines indicate the number densities of atomic H (solid lines) that originate from dissociation of H_2 molecules (dashed lines), based on H_2 surface number densities of $2.6 \times 10^7 \text{ cm}^{-3}$ and $5 \times 10^5 \text{ cm}^{-3}$, respectively.

96 [19]. Therefore, we assume that the ion production rate, given by the number of H atoms times the
 97 ionization rate, directly corresponds to the number density of freshly picked-up protons and that
 98 the ICWs are fully developed after 100 pick-up ion gyro periods.

99 Figure 3 shows the radial dependence of the estimated H number density, given in Mercury
 100 radii ($R_M = 2440 \text{ km}$). The black boxes represent the the median number densities of H and the
 101 upper/lower quartiles. The black error bars are the maximum and minimum densities within the
 102 $0.5 R_M$ bins. The obtained medians decrease from $\sim 830 \text{ cm}^{-3}$ to $\sim 80 \text{ cm}^{-3}$ between $2 R_M$ and
 103 $7.5 R_M$. The relationship is approximately logarithmic between number density and radial distance.
 104 Although the number densities from individual ICW events can vary considerably within the bins

105 (see error bars), the differences between the upper and lower quartiles are small.

106 The lines in Figure 3 show the results of a 1D upper atmosphere/exosphere model [13, 14] that
107 includes ionization, dissociation and recombination of the atomic and molecular hydrogen. As a
108 first step, we model the H₂ exospheric density profile under the so far typical assumption that the
109 surface number density of H₂ is $2.6 \times 10^7 \text{ cm}^{-3}$, given by the upper limits derived from the detection
110 threshold of the Mariner 10 occultation experiment (blue dashed line) [21, 28]. The resulting H₂
111 exospheric profile is comparable to those obtained previously from the application of kinetic Monte
112 Carlo model [51, 50].

113 The solid blue line shows the H density profile originating from the dissociated H₂ molecules,
114 which is assumed to be the major source of H. Apparently the H density is generally higher than the
115 results obtained from the in-situ ICW observations, indicating that the H₂ surface density should
116 be lower than $\sim 2.6 \times 10^7 \text{ cm}^{-3}$. In a second step, we model the atomic H profile that fits well to
117 the H corona densities that have been inferred from the ICW observations. The best results are
118 obtained for a H₂ surface density of $\sim 5 \times 10^5 \text{ cm}^{-3}$. The red lines correspond to the shifted H₂
119 and H profiles based on this lower H₂ surface density. The density of $\sim 5 \times 10^5 \text{ cm}^{-3}$ is two orders
120 of magnitude lower than the Mariner 10 occultation experiment detection threshold.

121 Discussion

122 So far, only remote measurements of hydrogen Lyman- α emissions have been used to evaluate the
123 hydrogen exosphere at Mercury. In this study we present for the first time the number density
124 profile of hydrogen in Mercury's exosphere, based on in-situ magnetic field measurements of ion
125 cyclotron waves (ICWs) by the MESSENGER spacecraft.

126 Therefore, we assume that the observed ICW wave energy exactly corresponds to the free en-
127 ergy in the ring-beam distribution of the pick-up ions [19]. Simulations, however, show that the
128 energy transfer from the ions to the waves might be 3-4 times smaller, because the energy is dis-
129 tributed between wave growth and ion heating [8]. Consequently, the number densities obtained
130 in this study might be underestimated. The variability of the energy transfer efficiency might also
131 result in the broad distribution of estimated number densities at similar radial radial distances
132 from Mercury (see black error bars in Figure 3). However, these simulations only consider a per-
133 pendicular pick-up geometry with a pure ring distribution in velocity space and no parallel relative
134 drift velocity. Due to the small cone angle between the interplanetary magnetic field and solar

135 wind velocity, the observed ICWs are rather generated under quasi-parallel pick-up configurations.
 136 Theoretical studies on the growth rates for parallel and perpendicular pick-up geometries suggest
 137 that perpendicular picked-up ions produce ICWs with low growth rates and that parallel picked-up
 138 ions generate ICWs with large growth rates [48, 49]. Therefore, the observed ICWs are most likely
 139 fully developed in less than the assumed 100 ion gyro periods. Together with the assumption that
 140 the photoionization/photodissociation rate is similar for different radial distances (Mercury's ten-
 141 uous exosphere is optically thin) the derived H density may thus be understood as a lower limit.
 142 Note that this density is still more than three orders of magnitude larger than predicted by recent
 143 exospheric models, which assume a thermal H atom population with dayside H atom surface den-
 144 sities of 23 cm^{-3} [21, 28]. We also checked that the obtained H density is rather independent of
 145 Mercury's distance to the Sun and/or the solar wind velocity, suggesting that the hydrogen source
 146 rate from Mercury is rather constant.

147 Usually, the sources and sinks for the H atoms are assumed to be related to the surface chemistry
 148 [36] caused by solar wind protons which are implanted in the surface regolith, where they diffuse
 149 and degas to the exosphere mainly as H_2 molecules [21, 42]. A number of exospheric models and
 150 computational simulations have been developed to explain these highly complex and interrelated
 151 source and loss processes to understand the composition of Mercury's exosphere [51, 25, 35, 52, 24].
 152 By assuming that the solar wind is the only source of H_2 , previous studies applied a simple scaling
 153 of the observed helium density to obtain an upper limit of solar wind related H_2 surface densities of
 154 $\sim 10^4 \text{ cm}^{-3}$ [21]. These studies estimated hydrogen amounts that are about two orders of magnitude
 155 lower compared to the expected surface saturation column densities of incident solar wind particles.
 156 This would indicate that H is not retained efficiently on Mercury's surface, so that the H density
 157 may even remain so low that the H_2 formation in the surface is inefficient [21]. Therefore, these
 158 studies suggested that photolysis of water (H_2O) molecules, stemming from the bombardment of
 159 micrometeorites [5, 21, 27, 28], may be a much more efficient source of H_2 than chemical reactions
 160 in the surface [24].

161 We can estimate the H_2O density at Mercury's surface by using the estimated flux of $1 \times$
 162 $10^8 \text{ cm}^{-2}\text{s}^{-1}$ of H_2O from the vaporization of micrometeorites [27]. If we scale the H_2O photodisso-
 163 ciation time for average solar activity at 1 AU [20] to Mercury's average orbital distance of 0.38 AU,
 164 we obtain $\sim 10^4 \text{ s}$. The average micrometeorite related column density of H_2O is then $1 \times 10^{12} \text{ cm}^{-2}$.
 165 By using an average temperature of 4000 K for the ejecta gas/water vapor [51] one obtains a scale
 166 height for micrometeorite related H_2O vapor of $\sim 500 \text{ km}$. This would yield a surface number

167 density of $2 \times 10^4 \text{ cm}^{-3}$. This value is lower than the upper limit of possible H_2O surface density
 168 of $1.5 \times 10^7 \text{ cm}^{-3}$, estimated by earlier studies [21]. However, there will also be a thermal H_2O
 169 population on Mercury, that is produced by surface reactions and evaporation from ice deposits on
 170 the nightside or from the planet's interior [21, 27, 27, 34, 12]. H_2O molecules will be dissociated
 171 in H and OH and $\sim 13\%$ will yield H_2 and O atoms [18, 21]. However, one can expect that OH
 172 and O atoms will react with surrounding H atoms and other OH molecules so that H_2O will be
 173 recycled [21, 28]. Photochemical reactions most likely enhance the lifetime of H_2O molecules near
 174 Mercury's surface by ~ 8 times [21]. Moreover, a fraction of OH will be adsorbed at the surface
 175 where it also reacts with H so that H_2O can be recycled near the surface too. Because of these
 176 chemical reactions, H atoms that originated from dissociation of H_2 molecules will not contribute
 177 largely to the H density near the planet. Most H atoms will be transformed into H_2O , via reactions
 178 with OH and O as long as their density is not too low. Previous studies showed that the number
 179 density of thermally released H_2O molecules decreases fast to negligible values above $1.3 R_M$. The
 180 hotter micrometeorite-related H_2O population reaches $2 R_M$ with a number density of a few cm^{-3} .
 181 Because of the decreasing availability of OH and O molecules at these distances, H atoms will not
 182 be efficiently removed by photochemical processes with these molecules. Although, H atoms (that
 183 originate from H_2O molecules that originate from vaporized micrometeorites) may contribute to the
 184 atomic H number densities, which we have inferred from the ICW observations at larger planetary
 185 distances, we expect that the main source of our derived H number densities between $2 - 8 R_M$ is
 186 the dissociation of H_2 molecules.

187 Here we present the results of an exospheric model, which includes ionization, dissociation and
 188 recombination processes. The simulation output that fits the observationally derived H density
 189 best, yields a H_2 surface density of $\sim 5 \times 10^5 \text{ cm}^{-3}$. Such an H_2 surface density yields a modeled
 190 atomic H density of $1300 - 70 \text{ cm}^{-3}$ between $2 - 8 R_M$ (solid red line in Figure 3) with an escape
 191 rate of dissociated H atoms of $\sim 6 \times 10^{25} \text{ s}^{-1}$. Although these densities are more than three orders
 192 of magnitude larger than estimated by previous models, they are still in good agreement with the
 193 upper limits of the Lyman- α radiances measured by the MESSENGER UVVS instrument: The
 194 radiance R is given in rayleigh by $4\pi R = gN/10^6$, where N is the column density and g the photon
 195 scattering coefficient (referred to as g -value). We assume g -value for hydrogen to be $\sim 10^{-2} \text{ s}^{-1}$
 196 [26]. $N \approx n_H \cdot h$ is related to the the scale height h and the exospheric hydrogen density n_h at the
 197 tangent point (point where the line-of-sight intersects the radial vector perpendicular). Therewith
 198 we are able to determine the expected radiance at a specific radial distance. By e -folding the

199 modeled H density in Figure 3 (red line) we estimate an h value of ~ 2500 km between 2 to $3 R_M$.
 200 With $n_H \approx 800 \text{ cm}^{-3}$ at $2.5 R_M$ we obtain a hydrogen Lyman- α radiance of $\sim 150 R$ at an altitude
 201 of ~ 3600 km above Mercury’s surface. This estimate is close to the measured radiance of $\sim 120 R$
 202 derived during the second MESSENGER flyby [43, 22], thus, indirectly confirming the obtained
 203 hydrogen densities determined by the ICW observations.

204 From our analysis, we constrain the so far unknown and overestimated H_2 surface number
 205 density to $\sim 5 \times 10^5 \text{ cm}^{-3}$. This value allows us to study in the future the details of the solar
 206 wind implantation into Mercury’s regolith that leads to H, H_2 , OH, H_2O production and exospheric
 207 release as well as H_2O photochemistry in the exosphere. It will give us the opportunity to investigate
 208 and separate the H_2O sources and sinks on the innermost planet of the solar system. We expect
 209 that future measurements by the BepiColombo mission, in particular by the STROFIO and PICAM
 210 instruments, will help refine our knowledge about Mercury’s exosphere.

211 Methods

212 Ion cyclotron wave identification criteria

213 To find pick-up ion generated ion cyclotron waves (ICWs) in the solar wind upstream of Mercury,
 214 we use the 20 Hz magnetic field observations of MESSENGER [40] between March 2011 and April
 215 2015. Based on an extended boundary dataset [47, 15], only time intervals when MESSENGER
 216 was in the solar wind are preselected. To identify potential ICWs, the following steps are applied
 217 to ~ 100 s long intervals:

- 218 1. Within each interval the magnetic field data are transformed into a mean-field-aligned (MFA)
 219 coordinate system, where the parallel component, $\hat{\mathbf{b}}_{\parallel} = \mathbf{B}_0/|\mathbf{B}_0|$, is given by the average
 220 magnetic field, $\mathbf{B}_0 = [B_{x,0}, B_{y,0}, B_{z,0}]$, and the perpendicular components in this coordinate
 221 system are chosen to be $\hat{\mathbf{b}}_{\perp 2} = \hat{\mathbf{b}}_{\parallel} \times [0, 0, 1]$ and $\hat{\mathbf{b}}_{\perp 1} = \hat{\mathbf{b}}_{\perp 2} \times \hat{\mathbf{b}}_{\parallel}$.
- 222 2. Each interval (2048 datapoints) is split into 7 sub-intervals of ~ 30 s (512 datapoints) with
 223 50% overlap. The magnetic field data of each sub-interval are Fourier transformed and the
 224 power spectral density matrix is evaluated.
- 225 3. The diagonal elements of the matrix give the in-phase power densities, parallel (P_{\parallel}) and
 226 perpendicular ($P_{\perp} = \frac{1}{2} \cdot (P_{\perp 1} + P_{\perp 2})$) to the mean magnetic field (\mathbf{B}_0). The off-diagonal
 227 elements of the matrix yield the out-of-phase cross powers, i.e., the field rotation sense around

228 the mean field. The complex off-diagonal elements of the spectral matrix are used to determine
 229 the ellipticity and the handedness of the observed wave [33, 16, 2, 38]. Negative/positive signs
 230 refer to left/right-handed polarization of the wave in the spacecraft frame.

231 4. To evaluate the coherency between the input signals in a particular frequency range and to
 232 obtain how stable the components are in phase, the degree of polarization (*DOP*) of each sub-
 233 interval is determined. 100 % indicates a pure state wave and values less than 70 % indicate
 234 noise [38].

235 The arithmetic means of the obtained power densities and ellipticities of the 7 sub-intervals are
 236 calculated. A crucial condition for ion cyclotron waves generated by local ion pick-up is that the
 237 observed wave frequency in the spacecraft frame is the same as in the plasma frame (no Doppler-
 238 shift) and thus close to the local proton gyrofrequency [11]. To provide a reliable identification, we
 239 calculate the proton gyrofrequency $f_{c,H^+} = qB_0/(2\pi m)$ and error range $\Delta f_{c,H^+} = q\sigma_B/(2\pi m)$, with
 240 proton mass m , charge q and the average and standard deviation of the magnetic field magnitude
 241 B_0 and σ_B , for each ~ 100 s time interval and apply the following criteria in the frequency range
 242 $\Delta F = [0.8 \cdot (f_{c,H^+} - \Delta f_{c,H^+}), f_{c,H^+} + \Delta f_{c,H^+}]$:

- 243 • The power density per component is integrated in the frequency range ΔF to account for
 244 power maxima just below the calculated gyro frequency. The ratio between the integrated
 245 perpendicular E_{\perp} and parallel fluctuations E_{\parallel} is evaluated and needs to be larger than 5:
 246 $E_{\perp}/E_{\parallel} > 5$.
- 247 • Within ΔF the ellipticity ϵ should be smaller than -0.5 , to ensure a left-handed polarization
 248 of the observed wave.
- 249 • The degree of polarization *DOP* of all sub-intervals is required to be larger than 0.7 within
 250 ΔF , to maintain large coherency of the observed wave and that the signal-to-noise ratio is
 251 high.
- 252 • The maximum of the perpendicular fluctuating field P_{\perp} is within the limits of ΔF , to ensure
 253 that the observed wave is dominated by the ion cyclotron mode.

254 Figure 4 depicts an example of an identified ion cyclotron wave. Panel (a) shows the magnetic
 255 field observation in mean-field-aligned (MFA) coordinates. The two perpendicular components (red
 256 and blue) are coherent and their fluctuations dominate over the parallel magnetic field variations

257 (green). This can be also seen in Panel (b) where the perpendicular component of the power
 258 spectral density (red) prevails over the parallel component (green), indicating that the observed
 259 wave is rather transverse than compressional around the proton cyclotron frequency $f_{c,H^+} = 0.43$ Hz
 260 (marked as solid black line). The area between the two dashed lines illustrates the integration
 261 frequency range ΔF , used to evaluate the power densities, ellipticity and degree of polarization.
 262 Panel (c) shows the hodogram in each plane of the MFA coordinate system for the time interval
 263 from Panel (a). The observed wave is almost circularly left-hand polarized with an estimated
 264 ellipticity of ~ -0.70 .

265 These selection criteria deliver 3969 time intervals for 4 years of MESSENGER solar wind
 266 observations.

267 **Injection velocity estimate**

268 We use a solar wind propagation model [41] (provided by the AMDA database) to get an approx-
 269 imate estimate of the plasma density and velocity of the solar wind during the ICW observation
 270 period. As the injection velocity (\mathbf{V}_{inj}) we use the aberrated solar velocity (\mathbf{V}_{SW}), modified by the
 271 orbital motion of Mercury ($\mathbf{V}_{\text{♄}}$) as provided by the Navigation and Ancillary Information Facility
 272 (NAIF) [1] $\mathbf{V}_{\text{inj}} = -\mathbf{V}_{\text{SW}} + \mathbf{V}_{\text{♄}}$. The injection velocity vector is also used to determine the solar
 273 zenith angle (SZA), which is used to select events dayside of the terminator ($\text{SZA} < 90^\circ$) [9]. From
 274 the 3969 preselected time intervals, 2247 pertain to observations dayside of the terminator. These
 275 2247 ICWs constitute the dataset for this study.

276 **Hydrogen density estimate from ICW observation**

277 The total free energy, E_{free} , which is required to excite cyclotron waves from a pick-up ion ring-beam
 278 distribution is approximately given by [19]:

$$E_{\text{free}} = \frac{1}{4} m_i n_{H^+} V_A V_{\text{inj}} [(1 + \cos(\alpha))^2 + (1 - \cos(\alpha))^2]. \quad (1)$$

279 Here, m_i and n_{H^+} are the mass and density of the pick-up ions, V_A is the local Alfvén velocity,
 280 calculated from the modeled solar wind density and the in-situ magnetic field measurements, V_{inj}
 281 is the plasma injection velocity and $\alpha(\mathbf{V}_{\text{inj}}, \mathbf{B}_0)$ is the pitch angle between the plasma injection
 282 velocity and background magnetic field.

283 Inverting Eq. (1) for n_{H^+} yields the pick-up ion density, under the assumption that the entire
 284 free energy of the ring-beam distribution is transferred to the wave and corresponds to the observed
 285 ICW energy, $E_{\text{free}} = E_{\perp}$ [10]; n_{H^+} is a lower limit for lower energy transfer rates.

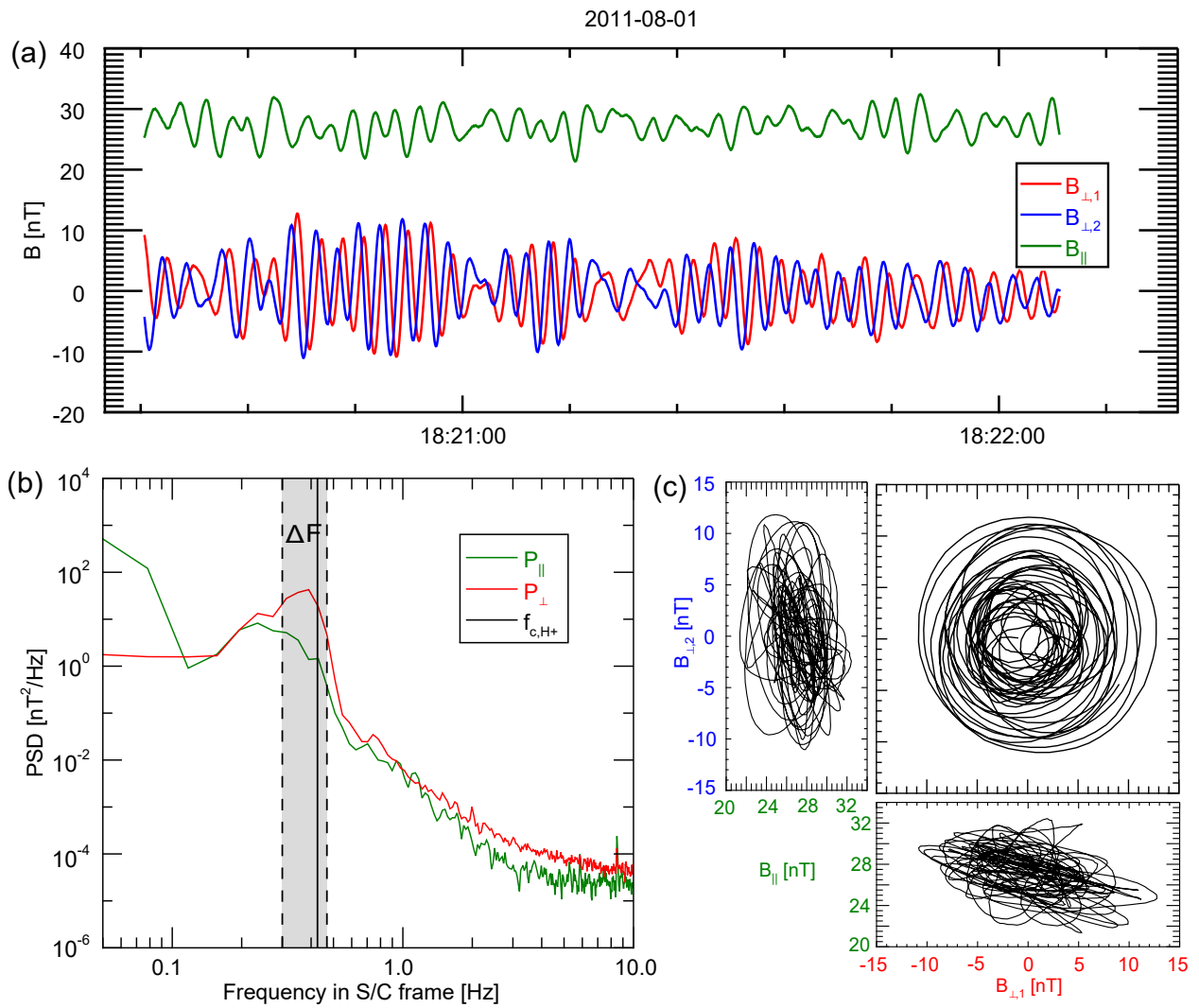


Figure 4: Example of an identified ion cyclotron wave (ICW). Panel (a) shows the magnetic field observations in mean-field-aligned (MFA) coordinates, (b) the power spectrum and (c) hodograms of the perpendicular and parallel magnetic field components.

Hybrid simulations have shown that the ICWs grow rapidly until a quasi-steady level is reached after 60 – 100 ion gyrations [7]. Under quasi-stationary conditions the freshly produced and lost ions are in equilibrium. Assuming that the full energy transfer from the ions to the waves takes 100 gyro periods, the pick-up ion density in this time should be balanced by the ion production rate, which can be estimated by multiplying the neutral hydrogen density n_{H} with the photoionization rate ν :

$$\frac{n_{\text{H}^+} 2\pi f_{\text{H}^+}}{100} = n_{\text{H}} \nu, \quad (2)$$

with n_{H^+} being the estimated pick-up ion density from Eq. (1) and f_{H^+} the gyrofrequency.

1D sub-/transonic upper atmosphere/exosphere model

In this study we apply a modified version of the 1D sub-/transonic upper atmosphere model introduced in previous publications [13, 14]. Taking into account that the Knudsen number is less than 1 at the surface, and the Jeans parameter $\lambda \approx 4.8$ for H_2 , we estimate the loss rate L , based on a modified Jeans escape formula, assuming a shifted Maxwellian particle distribution at the lower boundary:

$$L = \sqrt{\frac{k_{\text{B}} T_0}{2m_{\text{H}_2}}} \frac{N_0}{\sqrt{\pi}} F(u), \quad F(u) = \int_{\sqrt{\lambda}}^{\infty} [1 - (1 - 2uv)e^{2uv}] \frac{v}{u^2} e^{-v^2 - u^2} dv. \quad (3)$$

Here, k_{B} is the Boltzmann constant, m_{H_2} the mass of molecular hydrogen and T_0 and N_0 are the surface temperature and density. $F(u)$ is the velocity distribution function, with u the mean velocity normalized to the local thermal speed $\sqrt{2k_{\text{B}} \frac{T_0}{m_{\text{H}_2}}}$, determined by solving $u = F(u)$. In the limit $u = 0$, the function $F(u)$ is reduced to $F(u) = (1 + \lambda)e^{-\lambda}$, which yields the usual Jeans escape formula with λ the Jeans parameter given by $\frac{GMm_{\text{H}_2}}{k_{\text{B}}T_0R_{\text{M}}}$. Here, G is the gravitational constant and M and R_{M} are Mercury's mass and radius.

In the upper atmosphere model, we integrate a system of ordinary equations for dissociation and ionization from the planetary surface up to 8 Mercury radii. The obtained H_2 and H profiles include ionization, dissociation and recombination, given by

$$\begin{aligned} \frac{1}{r^2} L \frac{ds}{dr} &= \alpha_2 \xi_{\text{H}_2^+} \rho^2 (\xi_{\text{H}_2^+} + 2\xi_{\text{H}^+}) + \nu_{\text{d}} (1 - s - \xi_{\text{H}_2^+}) - 2\alpha_3 (s - \xi_{\text{H}^+})^2 (s + 1) \rho^3 \\ \frac{1}{r^2} L \frac{d\xi_{\text{H}_2^+}}{dr} &= \nu_{\text{i}2} \rho (1 - s - \xi_{\text{H}_2^+}) - \alpha_2 \xi_{\text{H}_2^+} (\xi_{\text{H}_2^+} + 2\xi_{\text{H}^+}) \rho^2 \\ \frac{1}{r^2} L \frac{d\xi_{\text{H}^+}}{dr} &= \nu_{\text{i}1} \rho (s - \xi_{\text{H}^+}) - \alpha_1 \xi_{\text{H}_2^+} (\xi_{\text{H}_2^+} + 2\xi_{\text{H}^+}) \rho^2 \end{aligned} \quad (4)$$

Here, ρ is the total mass density, s is the ratio of the atomic ($\text{H} + \text{H}^+$) and total mass density, ξ_{H^+} , $\xi_{\text{H}_2^+}$ are the mass fractions of the atomic (H^+) and molecular (H_2^+) ions, α_1 , α_2 and α_3 are the

310 coefficients of recombination ($\text{H}^+ + \text{e}^- \rightarrow \text{H}$), ($\text{H}_2^+ + \text{e}^- \rightarrow \text{H}_2$) and ($\text{H} + \text{H} \rightarrow \text{H}_2$), respectively, and
311 ν_{i1} , ν_{i2} and ν_d are rates of photoionization of H, H_2 and dissociation, respectively. Recombination
312 coefficients and ionization/dissociation rates are taken from previous publications [23, 53, 20].
313 Molecular hydrogen is considered to be the major constituent of the atmosphere and thus the total
314 mass density is assumed to be approximately equal to that of the H_2 density.

315 We further determine the density ρ -function by interpolating the H_2 profile from Monte Carlo
316 simulation H_2 results [50]. Using the determined loss rate L and density ρ , we integrate the system
317 of Eqs 4 with respect to quantities ξ_{H^+} , $\xi_{\text{H}_2^+}$ and s , which finally yields the radial distributions of
318 the dissociated atomic hydrogen and ionized particles.

319 Data availability

320 The magnetic field (MAG) data from the MESSENGER spacecraft are public available at the NASA
321 Planetary Data System (PDS) and can be retrieved on their website ([https://pds-ppi.igpp.
322 ucla.edu/search/view/?f=yes&id=pds://PPI/MESS-E_V_H_SW-MAG-4-SUMM-CALIBRATED-V1.0/
323 DATA/MSO](https://pds-ppi.igpp.ucla.edu/search/view/?f=yes&id=pds://PPI/MESS-E_V_H_SW-MAG-4-SUMM-CALIBRATED-V1.0/DATA/MSO)).

324 The solar wind density and velocity data were obtained from the AMDA database ([http://amda.
325 cdpp.eu/](http://amda.cdpp.eu/)). All data are open-access and can be downloaded on their website via the Workspace
326 Explorer under: Solar Wind Propagation Models/Mercury/Tao Model/SW/Input OMNI.

327 The orbital motion of Mercury were retrieved from the Navigation and Ancillary Information
328 Facility (NAIF), publicly accessible on the NASA Jet Propulsion Laboratory (JPL) webpage
329 (<https://wgc.jpl.nasa.gov:8443/webgeocalc/#StateVector>).

330 References

- 331 [1] C. H. Acton. Ancillary data services of NASA's Navigation and Ancillary Information Facility.
332 *Planet. Space Sci.*, 44(1):65–70, 1996.
- 333 [2] C. W. Arthur, R. L. McPherron, and J. D. Means. A comparative study of three techniques
334 for using the spectral matrix in wave analysis. *Radio Science*, 11(10):833–845, 1976.

- 335 [3] J. Bishop and J. W. Chamberlain. Radiation pressure dynamics in planetary exospheres: A
336 "natural" framework. *Icarus*, 81(1):145–163, 1989.
- 337 [4] A. L. Broadfoot, S. Kumar, M. J. S. Belton, and M. B. McElroy. Mercury's Atmosphere from
338 Mariner 10: Preliminary Results. *Science*, 185(4146):166–169, 1974.
- 339 [5] A. L. Broadfoot, D. E. Shemansky, and S. Kumar. Mariner 10: Mercury atmosphere. *Geophys.*
340 *Res. Lett.*, 3(10):577–580, 1976.
- 341 [6] J. W. Chamberlain. Planetary coronae and atmospheric evaporation. *Planet. Space Sci.*,
342 11(8):901–960, 1963.
- 343 [7] M. M. Cowee, S. P. Gary, and H. Y. Wei. Pickup ions and ion cyclotron wave amplitudes
344 upstream of Mars: First results from the 1D hybrid simulation. *Geophys. Res. Lett.*, 39(8),
345 2012.
- 346 [8] M. M. Cowee, D. Winske, C. T. Russell, and R. J. Strangeway. 1D hybrid simulations of
347 planetary ion-pickup: Energy partition. *Geophys. Res. Lett.*, 34(2), 2007.
- 348 [9] M. Delva, C. Mazelle, and C. Bertucci. Upstream Ion Cyclotron Waves at Venus and Mars.
349 *Space Sci. Rev.*, 162:25–24, 2011.
- 350 [10] M. Delva, M. Volwerk, C. Mazelle, J. Y. Chaufray, J. L. Bertaux, T. L. Zhang, and Z. Vörös.
351 Hydrogen in the extended Venus exosphere. *Geophys. Res. Lett.*, 36(1), 2009.
- 352 [11] M. Delva, T. L. Zhang, M. Volwerk, Z. Vörös, and S. A. Pope. Proton cyclotron waves in the
353 solar wind at Venus. *J. Geophys. Res: Planets*, 113(E9), 2008.
- 354 [12] A. N. Deutsch, J. W. Head, and G. Neumann. Age constraints of Mercury's polar deposits
355 suggest recent delivery of ice. *Earth and Planet. Sci. Lett.*, 520:26–33, 2019.
- 356 [13] N. V. Erkaev, H. Lammer, P. Odert, K. G. Kislyakova, C. P. Johnstone, M. Güdel, and
357 M. L. Khodachenko. EUV-driven mass-loss of protoplanetary cores with hydrogen-dominated
358 atmospheres: the influences of ionization and orbital distance. *MNRAS*, 460(2):1300–1309,
359 2016.
- 360 [14] N. V. Erkaev, P. Odert, H. Lammer, K. G. Kislyakova, L. Fossati, A. V. Mezentsev, C. P.
361 Johnstone, D. I. Kubyshkina, I. F. Shaikhislamov, and M. L. Khodachenko. Effect of stellar

- 362 wind induced magnetic fields on planetary obstacles of non-magnetized hot Jupiters. *MNRAS*,
363 470(4):4330–4336, 2017.
- 364 [15] W. Exner, S. Simon, D. Heyner, and U. Motschmann. Influence of Mercury’s Exosphere on
365 the Structure of the Magnetosphere. *J. Geophys. Res: Space Physics*, 125(7):e2019JA027691,
366 2020.
- 367 [16] R. A. Fowler, B. J. Kotick, and R. D. Elliott. Polarization analysis of natural and artificially
368 induced geomagnetic micropulsations. *J. Geophys. Res: Space Physics*, 72(11):2871–2883,
369 1967.
- 370 [17] S. P. Gary. Electromagnetic Ion / Ion Instabilities and Their Consequences in Space Plasmas
371 - a Review. *Space Sci. Rev.*, 56(3-4):373–415, may 1991.
- 372 [18] T. I. Gombosi, A. F. Nagy, and T. E. Cravens. Dust and neutral gas modeling of the inner
373 atmospheres of comets. *Reviews of Geophysics*, 24:667–700, 1986.
- 374 [19] D. E. Huddleston and A. D. Johnstone. Relationship between wave energy and free energy from
375 pickup ions in the comet Halley environment. *J. Geophys. Res: Space Physics*, 97(A8):12217–
376 12230, 1992.
- 377 [20] W. F. Huebner and J. Mhkerjee. Photoionization and photodissociation rates in solar and
378 black body radiation fields. *Planet. Space Sci.*, 106:11–45, 2015.
- 379 [21] D. M. Hunten, T. H. Morgan, and D. E. Shemansky. *The Mercury atmosphere*, pages 562–612,
380 1988.
- 381 [22] B. Ishak. Mercury: the view after MESSENGER. *Contemporary Physics*, 60(4):341–341, 2019.
- 382 [23] C. P. Johnstone, M. Güdel, A. Stökl, H. Lammer, L. Tu, K. G. Kislyakova, T. Lüftinger,
383 P. Odert, N. V. Erkaev, and E. A. Dorfi. The Evolution of Stellar Rotation and the Hydrogen
384 Atmospheres of Habitable-zone Terrestrial Planets. *Astrophys. J. Lett.*, 815(1):L12, 2015.
- 385 [24] B. M. Jones, M. Sarantos, and T. M. Orlando. A New In Situ Quasi-continuous Solar-wind
386 Source of Molecular Water on Mercury. *The Astrophysical Journal*, 891(2):L43, 2020.
- 387 [25] R. Killen, G. Cremonese, H. Lammer, S. Orsini, A. E. Potter, A. L. Sprague, P. Wurz, M. L.
388 Khodachenko, H. I. M. Lichtenegger, A. Milillo, and Mura. Processes that Promote and
389 Deplete the Exosphere of Mercury. *Space Sci. Rev.*, 132(2-4):433–509, 2007.

- 390 [26] R. Killen, D. Shemansky, and N. Mouawad. Expected Emission from Mercury's Exospheric
391 Species, and their Ultraviolet-Visible Signatures. *The Astrophysical Journal Supplement Series*,
392 181(2):351–359, 2009.
- 393 [27] R. M. Killen, J. Benkhoff, and T. H. Morgan. Mercury's Polar Caps and the Generation of an
394 OH Exosphere. *Icarus*, 125(1):195–211, 1997.
- 395 [28] R. M. Killen and W.-H. Ip. The surface-bounded atmospheres of Mercury and the Moon.
396 *Reviews of Geophysics*, 37(3):361–406, 1999.
- 397 [29] S. Kumar. Mercury's Atmosphere: A Perspective after Mariner 10. *Ikarus*, 28(4):579–591,
398 1976.
- 399 [30] C. Mazelle and F. M. Neubauer. Discrete wave packets at the proton cyclotron frequency at
400 comet P/Halley. *Geophys. Res. Lett.*, 20(2):153–156, 1993.
- 401 [31] C. Mazelle, D. Winterhalter, K. Sauer, J. G. Trotignon, M. H. Acuña, K. Baumgärtel,
402 C. Bertucci, D. A. Brain, S. H. Brecht, M. Delva, E. Dubinin, M. Øieroset, and J. Slavin.
403 Bow Shock and Upstream Phenomena at Mars. *Space Sci. Rev.*, 111(1):115–181, 2004.
- 404 [32] W. E. McClintock and M. R. Lankton. The Mercury Atmospheric and Surface Composition
405 Spectrometer for the MESSENGER Mission. *Space Sci. Rev.*, 131(1-4):481–521, 2007.
- 406 [33] J. D. Means. Use of the three-dimensional covariance matrix in analyzing the polarization
407 properties of plane waves. *J. Geophys. Res: Space Physics*, 77(28):5551–5559, 1972.
- 408 [34] J. I. Moses, K. Rawlins, K. Zahnle, and L. Dones. External Sources of Water for Mercury's
409 Putative Ice Deposits. *Icarus*, 137(2):197–221, 1999.
- 410 [35] A. Mura, A. Milillo, S. Orsini, and S. Massetti. Numerical and analytical model of Mercury's
411 exosphere: Dependence on surface and external conditions. *Planet. Space Sci.*, 55(11):1569–
412 1583, 2007.
- 413 [36] A. E. Potter. Chemical sputtering could produce sodium vapor and ice on Mercury. *Geophys.*
414 *Res. Lett.*, 22(23):3289–3292, 1995.
- 415 [37] C. Russell, S. Mayerberger, and X. Blanco-Cano. Proton cyclotron waves at Mars and Venus.
416 *Advances in Space Research*, 38(4):745–751, 2006.

- 417 [38] J. C. Samson and J. V. Olson. Some comments on the descriptions of the polarization states
418 of waves. *Geophysical Journal International*, 61(1):115–129, 04 1980.
- 419 [39] J. A. Slavin and R. E. Holzer. Solar wind flow about the terrestrial planets, 1. Modeling bow
420 shock position and shape. *J. Geophys. Res: Space Physics*, 86(A13):11401–11418, 1981.
- 421 [40] S. C. Solomon, R. L. McNutt, R. E. Gold, and D. L. Domingue. MESSENGER Mission
422 Overview. *Space Sci. Rev.*, 131:3–39, 2007.
- 423 [41] C. Tao, R. Kataoka, H. Fukunishi, Y. Takahashi, and T. Yokoyama. Magnetic field variations
424 in the jovian magnetotail induced by solar wind dynamic pressure enhancements. *J. Geophys.
425 Res: Space Physics*, 110(A11), 2005.
- 426 [42] O. J. Tucker, W. M. Farrell, R. M. Killen, and D. M. Hurley. Solar Wind Implantation Into
427 the Lunar Regolith: Monte Carlo Simulations of H Retention in a Surface With Defects and
428 the H₂ Exosphere. *J. Geophys. Res: Planets*, 124(2):278–293, 2019.
- 429 [43] R. J. Vervack, R. M. Killen, A. L. Sprague, M. H. Burger, A. W. Merkel, and M. Sarantos.
430 Early MESSENGER Results for Less Abundant or Weakly Emitting Species in Mercury’s
431 Exosphere. In *EPSC-DPS Joint Meeting 2011*, volume 2011, page 1131, 2011.
- 432 [44] R. J. Vervack, W. E. McClintock, E. T. Bradley, R. M. Killen, A. L. Sprague, N. Mouawad,
433 N. R. Izenberg, M. C. Kochte, and M. R. Lankton. MESSENGER Observations of Mercury’s
434 Exosphere: Discoveries and Surprises from the First Two Flybys. In *Lunar and Planetary
435 Science Conference*, Lunar and Planetary Science Conference, page 2220, 2009.
- 436 [45] R. J. Vervack, W. E. McClintock, R. M. Killen, A. L. Sprague, B. J. Anderson, M. H. Burger,
437 E. T. Bradley, N. Mouawad, S. C. Solomon, and N. R. Izenberg. Mercury’s Complex Exosphere:
438 Results from MESSENGER’s Third Flyby. *Science*, 329(5992):672–675, 2010.
- 439 [46] R. J. Vervack Jr., R. M. Killen, W. E. McClintock, A. W. Merkel, M. H. Burger, T. A. Cassidy,
440 and M. Sarantos. New discoveries from MESSENGER and insights into Mercury’s exosphere.
441 *Geophys. Res. Lett.*, 43(22):11,545–11,551, 2016.
- 442 [47] R. M. Winslow, B. Anderson, C. Johnson, J. Slavin, H. Korth, M. Purucker, D. N. Baker,
443 and S. Solomon. Mercury’s magnetopause and bow shock from MESSENGER Magnetometer
444 observations. *J. Geophys. Res: Space Physics*, 118:2213–2227, 2013.

- 445 [48] C. S. Wu and R. C. Davidson. Electromagnetic instabilities produced by neutral-particle
446 ionization in interplanetary space. *J. Geophys. Res: Space Physics*, 77(28):5399–5406, 1972.
- 447 [49] C. S. Wu, R. E. Hartle, and K. W. Ogilvie. Interaction of singly charged interstellar helium
448 ions with the solar wind. *J. Geophys. Res: Space Physics*, 78(1):306–309, 1973.
- 449 [50] P. Wurz, D. Gamborino, A. Vorburger, and J. M. Raines. Heavy Ion Composition of Mercury’s
450 Magnetosphere. *J. Geophys. Res: Space Physics*, 124(4):2603–2612, 2019.
- 451 [51] P. Wurz and H. Lammer. Monte-Carlo simulation of Mercury’s exosphere. *Icarus*, 164(1):1–13,
452 2003.
- 453 [52] P. Wurz, J. A. Whitby, U. Rohner, J. A. Martin-Fernandez, H. Lammer, and C. Kolb.
454 Self-consistent modelling of Mercury’s exosphere by sputtering, micro-meteorite impact and
455 photon-stimulated desorption. *Planetary and Space Science*, 58(12):1599–1616, 2010.
- 456 [53] R. V. Yelle. Aeronomy of extra-solar giant planets at small orbital distances. *Icarus*,
457 170(1):167–179, 2004.

458 **Acknowledgements**

459 We acknowledge the support from the Austrian Research Promotion Agency (FFG) ASAP MERMAG-
460 4 under contract 865967. We thank W. Heis for the help in illustrating the ion cyclotron wave
461 generation mechanism in Figure 1 and thank M. Delva for fruitful discussions.

462 **Author contributions**

463 D.S. initiated this study, did the analysis, and wrote the paper. F.P., M.V. contributed to the
464 analysis and interpretation of the results and helped editing the paper. N.V.E set up the simulation
465 and contributed the simulation results. W.B. and Y.N. gave valuable input to the manuscript. B.J.
466 guaranteed the quality of magnetic field data of MESSENGER. H.L. gave the initial idea of the
467 exospheric model used to explain the observationally derived results, and contributed to writing
468 and editing the manuscript.

469 **Additional information**

470 **Competing interests:** The authors declare no competing interests.

471 **Reprints and permission** information is available online at:

472 <http://npg.nature.com/reprintsandpermissions/>

Figures

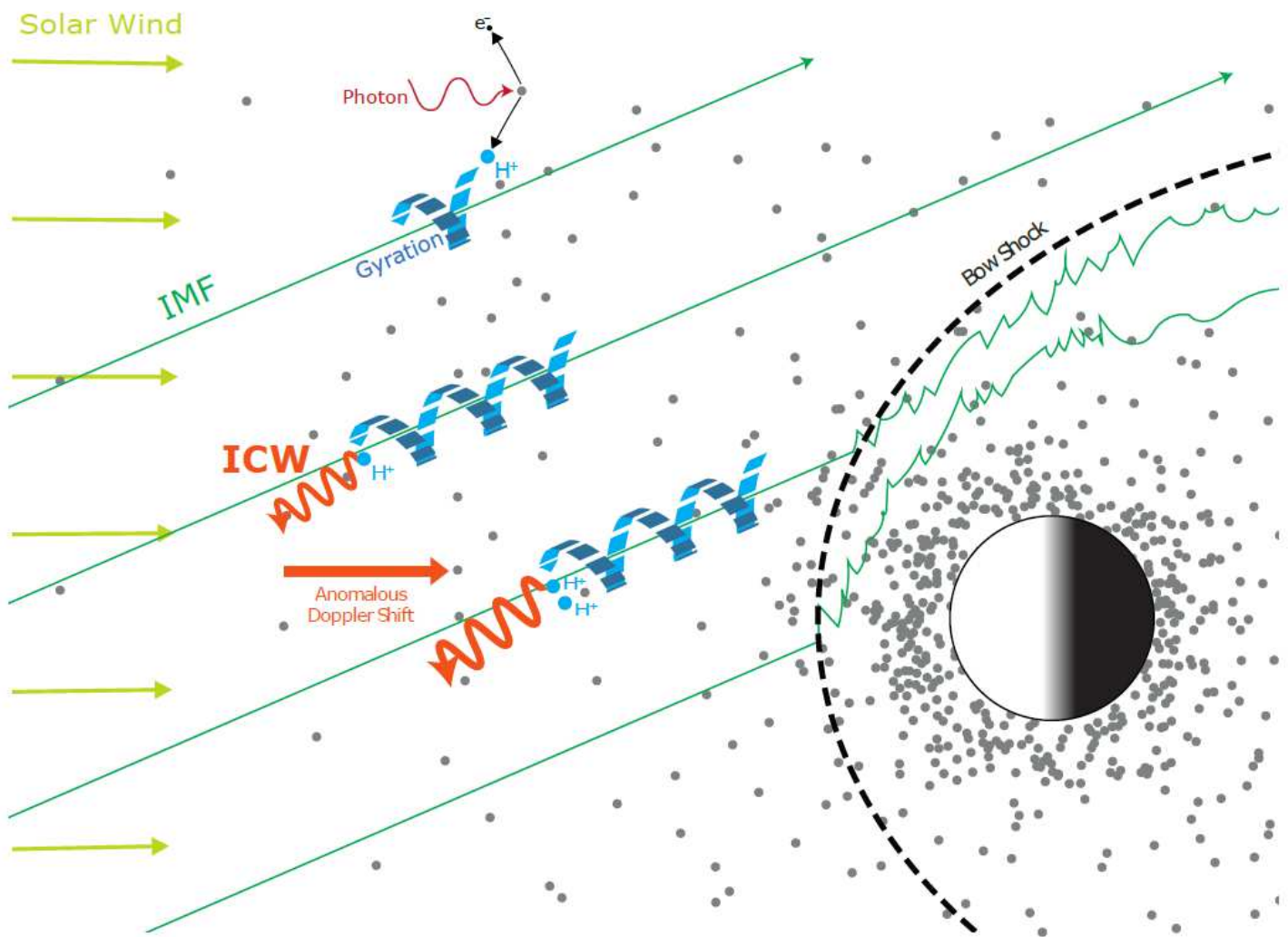
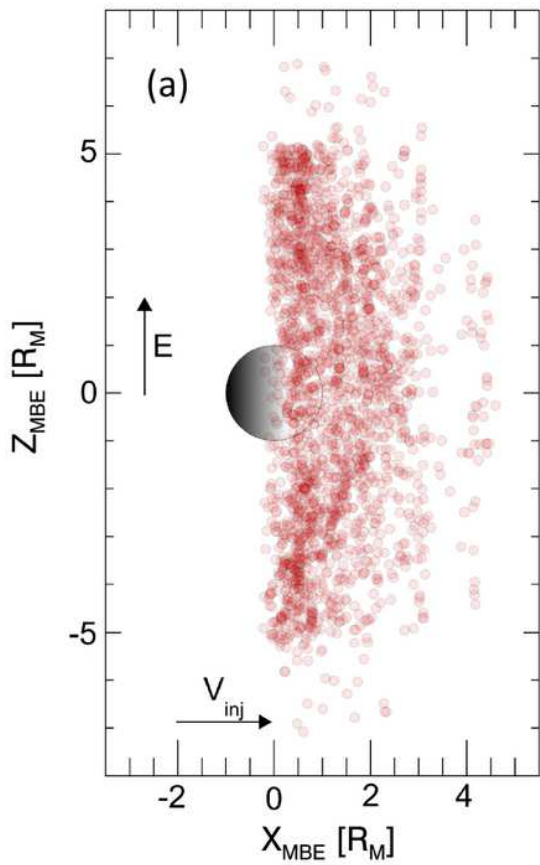


Figure 1

Illustration of ion cyclotron waves (ICWs, orange lines) generated by the gyration (blue lines) of protons (H^+ , blue dots) around the interplanetary magnetic field (IMF, green lines), which are created by photoionization of atomic hydrogen (H, grey dots).

Electromagnetic coordinate system



Normalized histogram of 2247 ICW

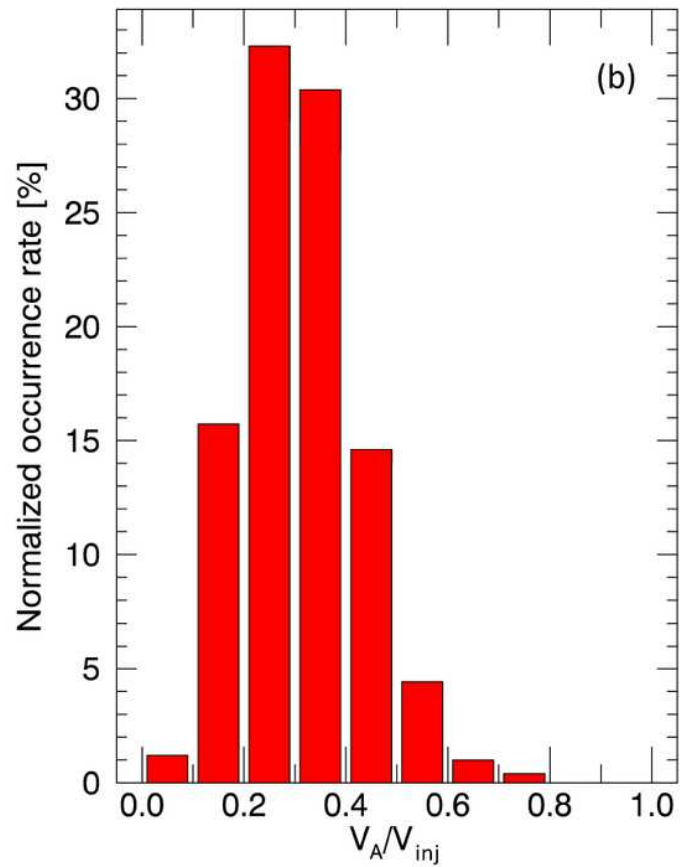


Figure 2

Panel (a) shows the position of the 2247 ion cyclotron waves (ICWs) in electromagnetic coordinates: X_{MBE} points sunward opposite to the solar wind velocity V_{inj} , Y_{MBE} is positive in direction of the mean magnetic field B_0 component perpendicular to X_{MBE} , and the Z_{MBE} axis is positive in direction of the convection electric field $E = V_{inj} \times B_0$. Panel (b) shows the normalized occurrence rate of estimated $V_A = V_{inj}$ ratios.

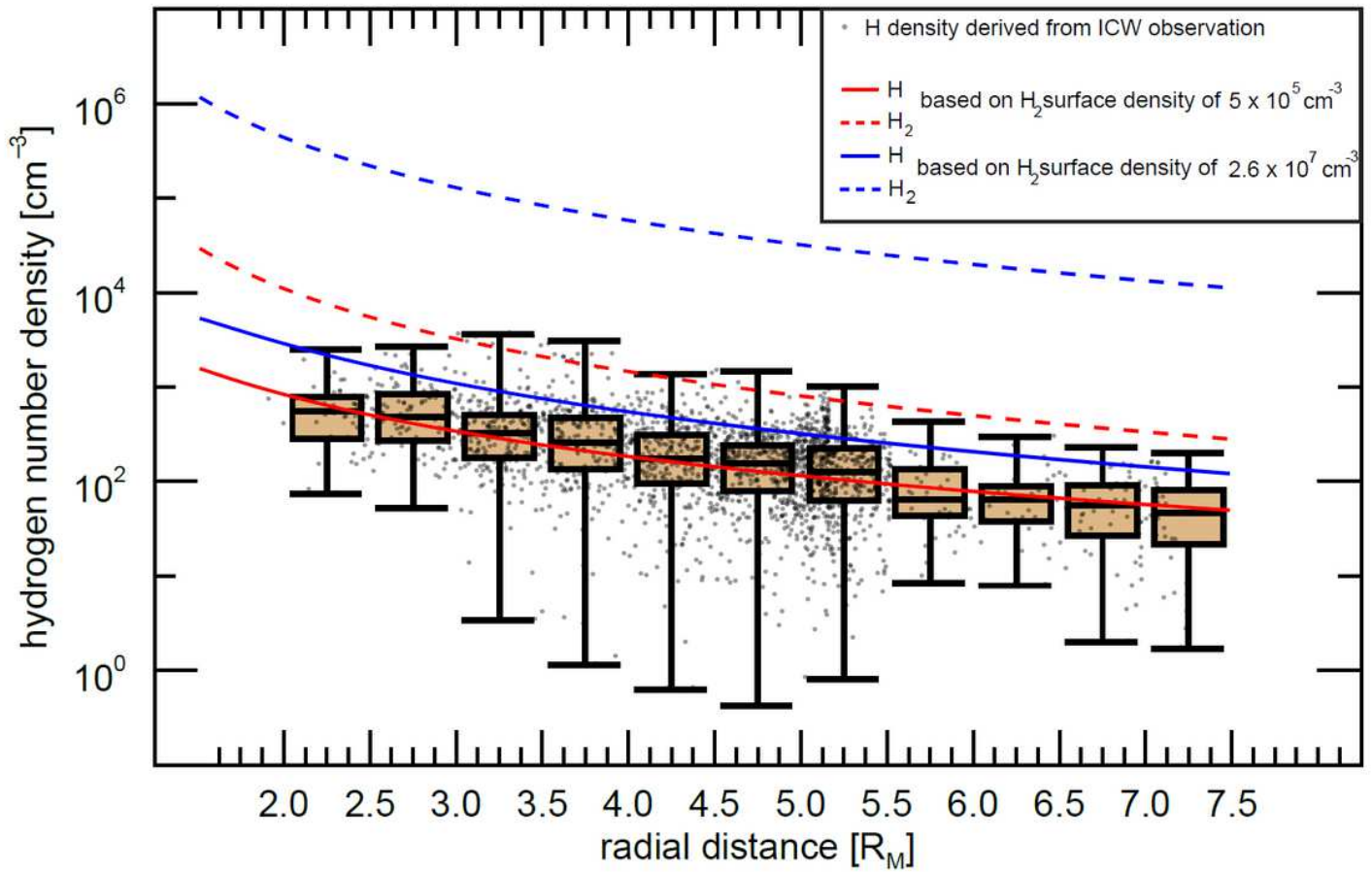


Figure 3

Boxplot of the estimated hydrogen densities as a function of the radial observation distance. The black error bar indicate the minimum and maximum number density within each 0:5RM bin. The boxes indicate the lower and upper quartiles and the horizontal black lines the median number density of each bin. The gray dots depict the derived hydrogen number densities of the 2247 ICW events. The blue and red lines indicate the number densities of atomic H (solid lines) that originate from dissociation of H₂ molecules (dashed lines), based on H₂ surface number densities of $2.6 \times 10^7 \text{ cm}^{-3}$ and $5 \times 10^5 \text{ cm}^{-3}$, respectively.

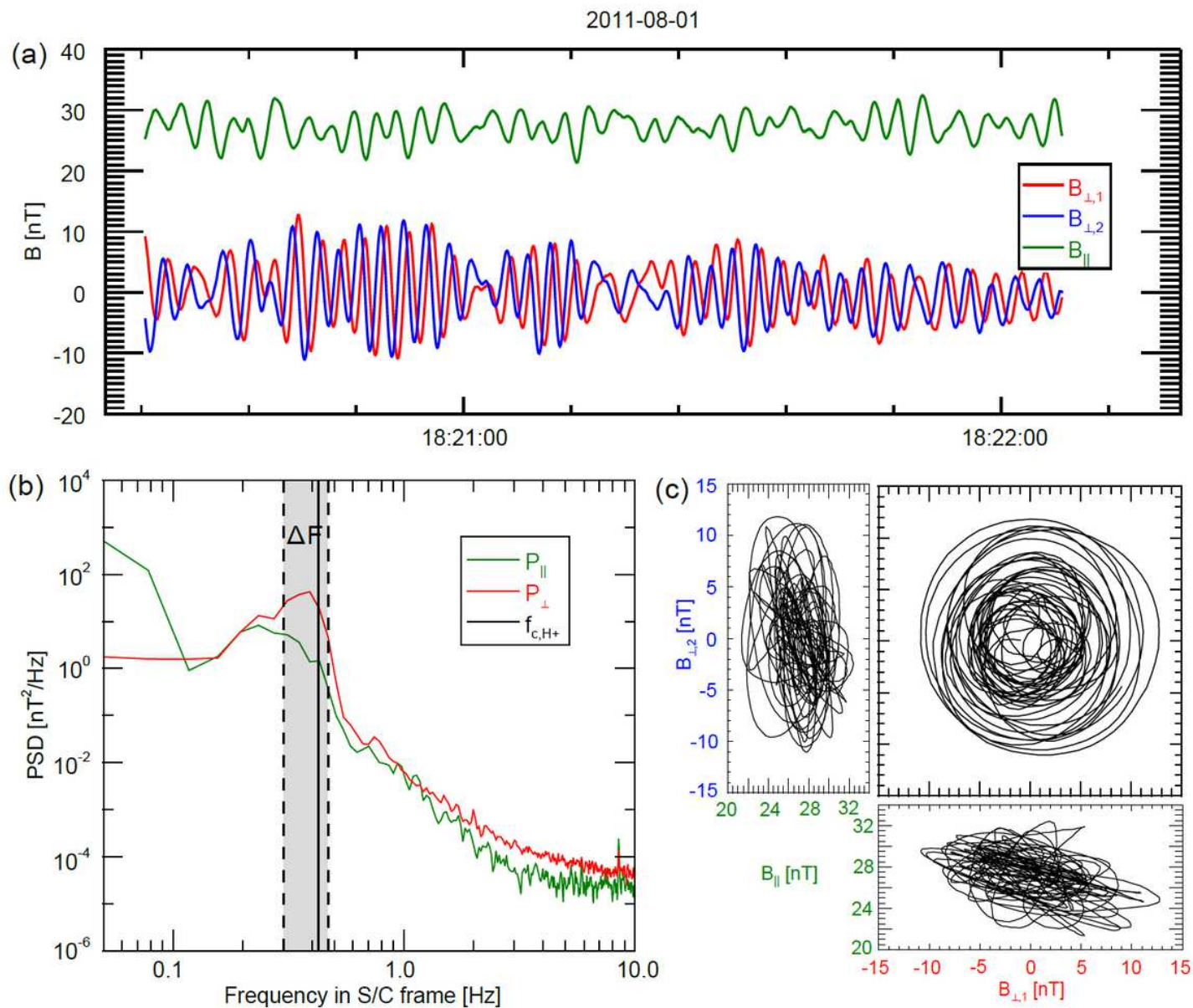


Figure 4

Example of an identified ion cyclotron wave (ICW). Panel (a) shows the magnetic field observations in mean-field-aligned (MFA) coordinates, (b) the power spectrum and (c) hodograms of the perpendicular and parallel magnetic field components.